Nano Research

Open Access

Research Article

Engineering Fe–Pt dual atomic sites for efficient electrooxidation of benzyl alcohol via a tandem water oxidation process at Ampere-level current density

Gaohang Song, Wenming Sun, Xiaolu Wang ✉, Shuyan Gong, and Yang Tian ✉

Department of Chemistry, Capital Normal University, Beijing 100048, China

Cite this article: *Nano Research*, **2025**, *18*, 94907362. https://doi.org/10.26599/NR.2025.94907362

ABSTRACT: Active oxygen radicals (OH*/O*/OOH*) generated from oxygen evolution reaction (OER) play a crucial role in facilitating the electrooxidation of organic compounds into high value-added chemicals. However, constructing atomically precise active sites with a specific function to catalyze water-coupled electrooxidation reactions in a tandem system still confronts a great challenge. Herein, we propose a novel water-participating benzyl alcohol electrooxidation tandem process by constructing homogeneous isolated Fe–Pt dual-atom site catalysts on CoOOH nanosheet arrays (FePt DAC). The Fe and Pt dual atomic sites synergistically deliver excellent benzyl alcohol oxidation reaction activity with a high current density of 1500 mA·cm^{-2} at a low potential of 1.49 V (vs. reversible hydrogen electrode (RHE)) and remarkable long-term durability without obvious attenuation after 530 h operation. *In-situ* Fourier-transform infrared spectroscopy, isotopic tracing experiment, and detailed theoretical calculations further reveal the tandem mechanism, in which the *in-situ* generated O* species on the Fe site through OER process serve as key intermediates that bridge the subsequent electrochemical benzyl alcohol oxidation on neighboring Pt site. This coupled oxidation mechanism turns competitive OER process into mutual benefits and provides insights to achieve directional transformation of chemical bonds via construction of collaborative dual atomic sites.

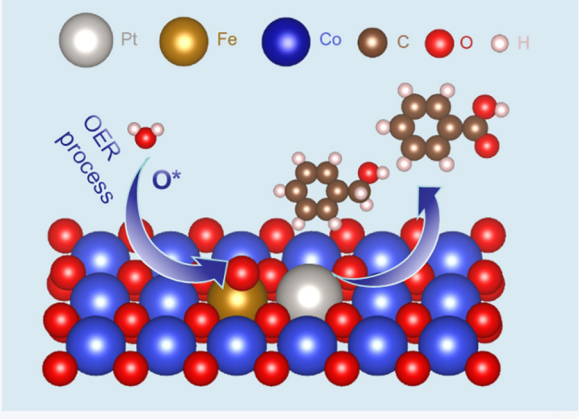

KEYWORDS: dual atomic sites, coupled oxidation, tandem catalysis, oxygen evolution reaction, benzyl alcohol oxidation

1 Introduction

The "green hydrogen" produced by water electrolysis that is driven by renewable energy is the only type of hydrogen that has the potential to achieve net zero carbon emissions throughout the entire process from production to consumption [1, 2]. Nevertheless, the conventional water electrolysis process requires a high working voltage (> 1.23 V) due to the inherently sluggish four-electron transfer of anodic oxygen evolution reaction (OER) [3, 4]. Various reactive oxygen intermediates (*OH, *O, OOH*) generated during the OER process are prone to bind with protons in the solution, thus inhibiting hydrogen evolution and thus reducing Faraday efficiency [5]. If those active oxygen intermediates that possess active chemical properties and strong oxidation ability [6–10] are used as oxygen source to participate in the electrooxidation, it is not only expected to achieve green synthesis of value-added bulk chemicals [11–13] but also to reduce anodic oxidation potential and overall energy consumption, facilitating hydrogen production at industrial scale [14, 15]. Among possible OER-substituted anodic reactions, alcohols can undergo oxidation by these active oxygen species, yielding aldehydes and acids [16, 17]. For example, the oxidation of benzyl alcohol produces benzoic acid, a valuable fine chemical that can be used in the synthesis of fibers, resins, and corrosion-resistant industries [18, 19]. However, water electrolysis coupled benzyl alcohol oxidation reaction (BAOR) involves multiple steps of electron and proton transfer [20–22]. Precise synthesis of electrocatalyst is the key to achieving high current density and targeted conversion of chemical bond.

The concept of single-atom catalyst (SAC) has sparked rapid development over a decade since its proposal in 2011 [23]. Attributing to its maximum atomic utilization, well-defined active

Received: January 29, 2025; **Revised:** March 9, 2025
Accepted: March 11, 2025

✉Address correspondence to Xiaolu Wang, 7088@cnu.edu.cn; Yang Tian, tianyang@cnu.edu.cn

sites and unsaturated coordination configurations, SAC exhibits significant foreground in various reactions [24–27]. However, it is difficult for SAC to break the linear relationship between different intermediates when the reaction involves multiple intermediates or requires more than one atom, limiting their application in tandem reactions [28–30]. For water-benzyl alcohol coupled oxidation system, it is essential for active oxygen intermediates generated by water oxidation to be matched with the subsequent adsorption, mass transfer, and oxidation process of organic compounds at the electrode interface. However, the optimal catalytic sites for these two processes may have completely different properties [31]. Hence, dual-atom site catalysts (DACs), as one step further in regulating SACs, have gained great attention in recent years [32–35]. The introduction of another metal atom into the active moiety of SACs, thus forming DACs, could help DACs inherit the high atomic utilization, atomic dispersity, and selectivity of SACs and also break the inherent limitation of the linear relationship [36–40]. These DACs catalysts offer more active sites to absorb and bind with the intermediates, tuning the binding mode via O-, C-, and N-binding sites, which give priority to fulfill complex reaction paths [41–44]. Yet, there is currently relatively little research on the use of DACs for water-coupled electrooxidation reactions.

Herein, we synthesized a DAC with atomically Fe and Pt homogeneously distributed on the CoOOH nanosheets (FePt DAC) through an electrochemical deposition strategy. The FePt DAC exhibited excellent benzyl alcohol electrooxidation activity with high current density (100 mA·cm^{-2} at 1.28 V vs. reversible hydrogen electrode (RHE) and 1500 mA·cm^{-2} at 1.49 V vs. RHE) and nearly 100% conversion to benzoic acid. Moreover, stability assessment over 500 h also implied a highly robust catalyst. *In-situ* spectrum and isotope-labeled method indicated the presence of oxygen radicals and the participation of H_2O in the formation of ultimate product. Detailed density functional theoretical (DFT) calculations further unveiled the tandem mechanism, showing the active O* radicals that are generated on the Fe site bridge OER process and the oxidation of benzyl alcohol. Specifically, the Fe atoms in the CoOOH lattice facilitate water oxidation, resulting in active O* radicals to oxidize the benzyl alcohol that was adsorbed on the adjacent Pt atoms, eventually generating benzoic acid. This work provided a new approach for the development of water electrolysis coupled oxidation and outlook to achieve the electrocatalytic oxidation of organics without external oxygen source through devising efficiently catalytic dual atomic sites to fulfil the industrial-scale production.

2 Results and discussion

2.1 Synthetic process and structure characterization of the FePt DAC

The CoOOH nanosheet was fabricated on nickel foam (NF) via electrodeposition in a standard three-electrode system followed by electroactivation (Figs. S1(a), S1(b), and S2(a) in the Electronic Supplementary Material (ESM)). Then, atomically dispersed Fe and Pt were successively loaded onto CoOOH substrate through a two-step electrodeposition strategy to obtain the final catalyst FePt DAC (Fig. 1(a)). After incorporating Fe and Pt, the hierarchical nanosheet arrays were well-retained without phase transition or perceptible morphological changes (Fig. 1(b) and Figs. S1(c)–S1(d) in the ESM). High-angle annual dark-field scanning transmission electron microscope (HAADF-STEM) images and corresponding energy-dispersive X-ray spectroscopy (EDS) element mapping images demonstrated the homogeneous distribution of Co, Fe, and Pt throughout the FePt DAC nanosheets (Fig. 1(c)). High-resolution TEM (HRTEM) image did not show visible metallic Fe or Pt species in FePt DAC (Fig. 1(d)). The corresponding selected area electron diffraction (SAED) pattern confirmed the existence of typical lattice facets of 0.142 and 0.243 nm that correspond to the

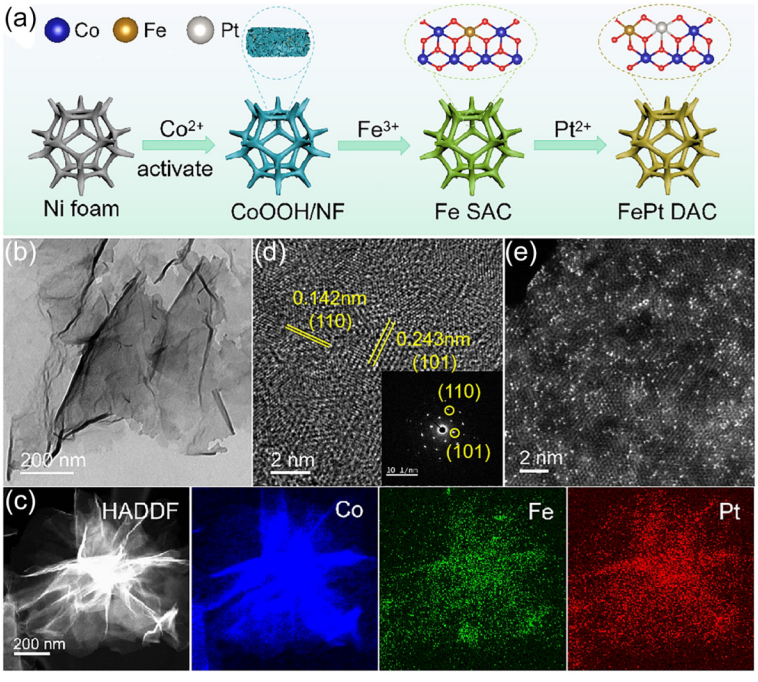

Figure 1 Schematic synthesis and structural characterization of FePt DAC catalyst. (a) Schematic illustration of the fabrication process of FePt DAC. (b) TEM image of FePt DAC. (c) EDS elemental mapping images of FePt DAC. (d) HRTEM image of FePt DAC. Inset was SAED pattern of FePt DAC. (e) Atomic-resolution HAADF-STEM image of FePt DAC.

(110) and (101) crystallographic planes of γ-CoOOH (PDF # 06-0075) (Fig. 1(d) and Fig. S3 in the ESM) [45, 46]. Those observations were consistent with the results of X-ray diffraction (XRD), which only displayed two typical peaks associated with the (003) and (006) planes of γ-CoOOH and no peaks of metal nanoparticles were observed [18]. Atomic-resolution HAADF-STEM image in Fig. 1(e) showed many isolated bright dots scattered on the CoOOH substrate that attributed to Pt atoms since Fe and Co atoms were not easily distinguishable because of their closer atomic numbers while Pt atoms were relatively heavier in contrast to the Co and Fe. Electron energy loss spectroscopy also proved the existence of Fe atoms (Fig. S4 in the ESM). In addition, the presence of Fe and Pt was further confirmed by inductively coupled plasma optical emissions spectrometry (ICP-OES) with 2.1 wt.% Fe and 4.3 wt.% Pt on the CoOOH supports, respectively (see Table S1 in the ESM). For comparison, we also prepared Fe SAC, Pt SAC, and PtFe DAC catalysts (Figs. S2(b)–S2(d) and S3 in the ESM). Particularly, the PtFe DAC was synthesized via changing the sequence of electrodeposition (see details in the ESM). The PtFe DAC exhibited similar hierarchical nanosheet morphology, as well as homogeneous Fe, Co, and Pt element distribution (Fig. S5 in the ESM). ICP data (see Table S1 in the ESM) exposed a decrease in Pt atom content (2.5 wt.%) compared to FePt DAC, which may account for the sharply decreased Pt atoms observed in the atomic-resolution HAADF-STEM image (Fig. S5(d) in the ESM).

2.2 Atomic structure and electronic state analysis of the FePt DAC

To examine the electronic and geometric structure evolution after the formation of FePt DAC, X-ray absorption spectroscopy (XAS) and X-ray photoelectron spectroscopy (XPS) spectra were conducted. The Fourier-transformed (FT) Fe K-edge extended X-ray absorption fine structure (EXAFS) spectra of FePt DAC exhibited an obvious peak at 1.47 Å, ascribing to the Fe–O coordination in the first shell (Fig. 2(a)). Wavelet transform (WT) plots for the Fe K-edge k^3-weighted EXAFS spectra evidenced the existence of Fe–O scattering path in FePt DAC with intensity maximum located at 5.23 $Å^{-1}$ (Fig. S6 in the ESM). The Pt L-edge FT-EXAFS spectra of FePt DAC showed a peak situated at 1.62 Å (Fig. 2(b)), which was assigned to the Pt–O stretching path in the first shell. In addition, as for Pt L-edge k^3-weighted EXAFS spectra, the WT-EXAFS plots were in agreement with the FT-EXAFS spectra, with the intensity maximum for Pt–O scattering path that situated at 6.03 $Å^{-1}$ in the *R*-space (Fig. S7 in the ESM). Contrastingly, no Fe–Fe or Pt–Pt scattering paths were observed in the FT-EXAFS and WT-EXAFS spectra. These results indicated the atomically dispersed Fe and Pt without clusters or nanoparticles. The FT-EXAFS spectra of Co K-edge showed that CoOOH and FePt DAC have similar double peaks at 1.44 and 2.42 Å, corresponding to Co–O and Co–O–Co, respectively (Fig. S8 in the ESM) [47]. Similar conclusion was found in the FT-EXAFS spectra of Co K-edge (Fig. S9 in the ESM).

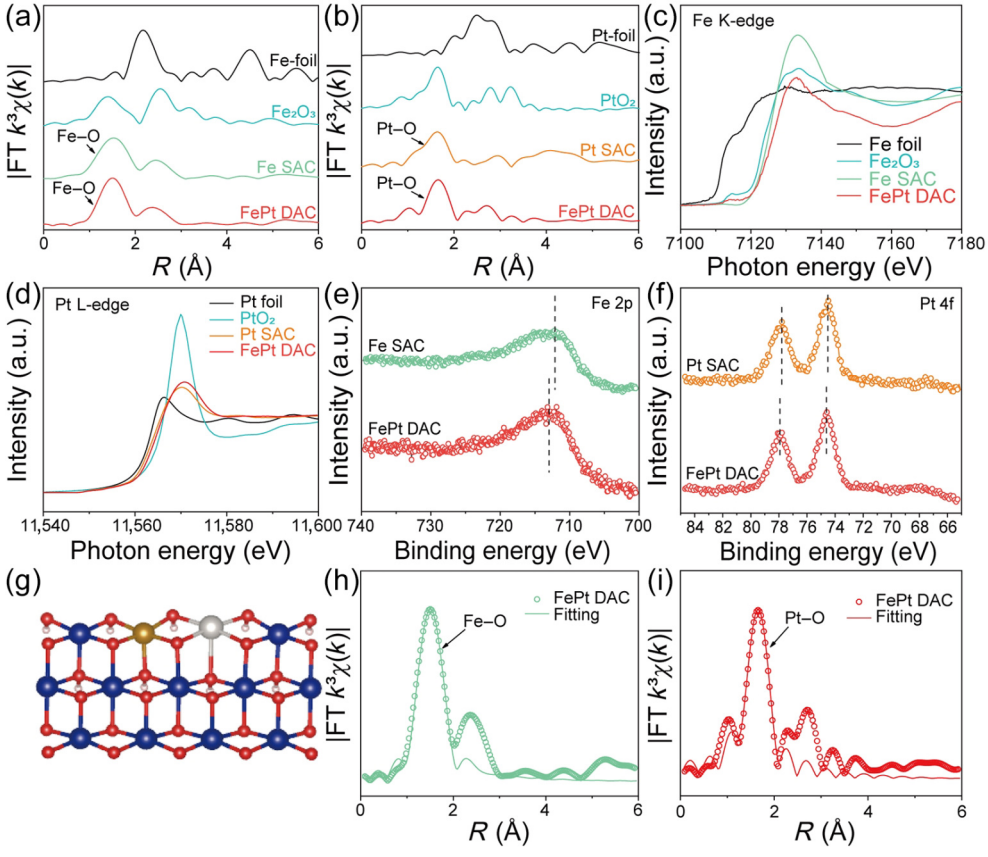

Figure 2 Electronic structure characterizations of FePt DAC. (a) FT-EXAFS spectra of Fe foil, Fe_2O_3, Fe SAC, and FePt DAC at Fe K-edge. (b) FT-EXAFS spectra of Pt foil, PtO_2, Pt SAC, and FePt DAC at Pt L-edge. (c) XANES spectra of Fe K-edge in Fe foil, Fe_2O_3, Fe SAC, and FePt DAC. (d) XANES spectra of Pt L-edge in Pt foil, PtO_2, Pt SAC, and FePt DAC. (e) Fe 2p XPS spectra of Fe SAC and FePt DAC. (f) Pt 4f XPS spectra of Pt SAC and FePt DAC. (g) Theoretical model of FePt DAC, in which yellow ball for Fe atom, gray ball for Pt atom, and indigo ball for Co atom. ((h) and (i)) EXAFS fitting results of FePt DAC in the first shell in *R*-space for (h) Fe K-edge and (i) Pt L-edge.

Fe K-edge X-ray absorption near-edge structure (XANES) spectra showed that the valence state of Fe in Fe SAC was higher than Fe foil and close to the Fe_2O_3, indicative of its valence state approaching Fe^{3+}. Specifically, when subsequently electrodeposition with Pt, the valence state of Fe continued to increase, suggesting the decreased Fe 3d electron density influenced by Pt atom doping (Fig. 2(c)). The valence fitting displayed its oxidation state of about +3.7 (Fig. S10 in the ESM). On the other side, the adsorption energy of Pt L-edge denoted that the adsorption edge of FePt DAC was situated between Pt foil and PtO_2, which meant the oxidation state of Pt was in the range of 0–+4 (Fig. 2(d)). The valence fitting displayed its oxidation state of about +1.7 (Fig. S11 in the ESM). In fact, compared with Pt SAC, Fe doping further increased the valence state of Pt. This was consistent with the valence state analysis for Fe mentioned above, where the electron cloud density of both Fe and Pt in the dual atom co-doped sample (FePt DAC) was reduced when compared with the Fe SAC and Pt SAC. Moreover, the K-edge XANES spectra of Co verified the decrease of the valence state of the substrate Co after loading the Fe atoms and Pt atoms (Fig. S12 in the ESM). These analysis results could be explained by the local structural disorder induced by atomic rearrangement during the formation of dual atomic site catalyst and the resulting charge redistribution between the Fe, Pt, and Co.

In addition, we further characterized the atomic-site structures of FePt DAC through the XPS results. The Fe 2p XPS spectra of FePt DAC had a high-energy shift of 0.8 eV compared with the Fe SAC catalyst (Fig. 2(e)). This meant that the valence state of Fe atom in FePt DAC was higher than Fe SAC, which was consistent with EXAFS results (Fig. 2(c)). The Pt 4f XPS spectra of FePt DAC displayed higher binding energy than that of Pt SAC catalyst (Fig. 2(f)), suggesting improved oxidation state of Pt in the FePt DAC, which coincided with the EXAFS results (Fig. 2(d)). Meanwhile, the Co 2p and deconvoluted components of the O 1s signal of FePt DAC, including lattice O (529 eV) and O in hydroxyl group or defective oxygen species (530.1 eV), showed lower binding energies than that of CoOOH (Fig. S13 in the ESM). From another perspective, the introduction of atomic Fe and Pt into CoOOH lattice definitely generated strong electronic metal–support interaction (EMSI) in the FePt DAC [48]. Finally, quantitative EXAFS fitting results revealed that the average coordination numbers of Fe–O and Pt–O in the first shell were 5.2 and 4.9, respectively in FePt DAC (Figs. 2(g)–2(i) and Table S2 in the ESM). These results implied that the formation of atomically scattered Fe and Pt sites into CoOOH carrier will induce the charge redistribution and electronic and coordination evolution of FePt DAC, which may have a positive effect on the enhancement of electrochemical BAOR performance.

2.3 Electrochemical performance of BAOR

The BAOR performance of FePt DAC was recorded and compared with those related samples in 1.0 M KOH solution with 0.1 M benzyl alcohol using a conventional three-electrode electrolytic cell. In addition, the OER activity of FePt DAC without the addition of benzyl alcohol was also assessed for comparison. As demonstrated in Fig. 3(a), FePt DAC exhibited high-catalytic current density of 100 $mA·cm^{-2}$ beyond 1.49 V for OER. Excitedly, upon the addition of 0.1 M benzyl alcohol, the FePt DAC delivered the catalytically most active polarization curve with a huge increase in current density. Specifically, FePt DAC exhibited a low potential of 1.28 V to reach a current density of 100 $mA·cm^{-2}$ in 1 M KOH solution with 0.1 M benzyl alcohol, which was 70 and 74 mV smaller than Fe SAC and Pt SAC (Fig. 3(a) and Table S3 in the ESM). Notably, the PtFe DAC with fewer Pt/Fe atom ratio also displayed inferior BAOR performance as compared with FePt DAC, but still outperformed Fe SAC and Pt SAC those samples without Fe and Pt dual atomic sites. The potential gap further increased to 220, 380, and 190 mV when the current density reached 1000 $mA·cm^{-2}$ (Fig. 3(b)). Impressively, when applied an external voltage of 1.52 V, the current density for FePt DAC reached 1750 $mA·cm^{-2}$, which was 2.8, 3, and 4.5 times that of PtFe DAC, Fe SAC, and Pt SAC, respectively, suggesting the superiority of FePt DAC in catalyzing benzyl alcohol. As presented in Fig. S14 in the ESM, the concentration of the benzyl alcohol rapidly declined prolonging the reaction time accompanied by the concentration increase of the benzoic acid product. Note that the product of benzaldehyde was initially detected and subsequently consumed (after 30 min) with the extension of reaction time, ascribing to its conversion into benzoic acid. After conducting the oxidation reaction for 180 min, benzyl alcohol was completely oxidized into benzoic acid with a high selectivity of up to 99% (Fig. S15 in the ESM). In addition, the enhanced BAOR kinetics can also be realized by the formation of dual atomic doping of Fe and Pt atoms in FePt DAC, which can be inferred by the much smaller Tafel slope of FePt DAC (47 $mV·dec^{-1}$) than Fe SAC (84 $mV·dec^{-1}$) and Pt SAC (86 $mV·dec^{-1}$) (Fig. 3(c)). Consequently, to our best knowledge, the overall BAOR performance of FePt DAC was superior to most reported electrocatalysts in references (Fig. 3(d) and Table S5 in the ESM).

To reveal the underlying BAOR mechanism, *operando* electrochemical impedance spectroscopy (EIS) spectra were conducted in 1 M KOH with and without 0.1 M benzyl alcohol, which has been regarded as an effective characterization tool to track the dynamic interface kinetics, electronic transfer, and mass transfer evolution of catalyst during the catalytic process [49–51]. As indicated in Fig. 3(e), a transition phase peak in the low-frequency region, usually related to the nonhomogeneous charge distribution caused by the OER, was observed at 1.45 V, suggesting the occurrence of the OER. Correspondingly, it also found that there was an apparent dropping of charge transfer resistance (R_{ct}) after 1.47 V (Fig. S16(a) in the ESM), demonstrating the onset of OER, well consistent with the corresponding linear scanning voltammetry (LSV) curves. On the other side, an obvious phase peak response was illustrated in the low-frequency region when the voltage reached 1.25 V in 1 M KOH with 0.1 M benzyl alcohol (Fig. 3(f)), which could be related to the BAOR, in accordance with the R_{ct} and LSV curves (Fig. S16(b) in the ESM). The significant decrease in inflection point demonstrated that the FePt DAC catalyst possessed faster kinetics in the BAOR. More importantly, chronopotentiometry (CP) measurement declared that FePt DAC also delivered outstanding stability at a current density of 10 $mA·cm^{-2}$ for more than 500 h without significant attenuation (Fig. 3(g)), which was significantly superior to the Fe SAC and Pt SAC (Fig. S17 in the ESM). The exceptional durability could be attributed to the outstanding structural stability of FePt DAC, evidenced by the well-maintained morphology and crystal structure (Fig. S18 in the ESM).

2.4 *In-situ* spectrum and reaction mechanism analysis

The *operando* Raman spectroscopy was then conducted at various potentials to examine the dynamic evolution mechanisms of FePt DAC during the BAOR process (Fig. S19 in the ESM). The *ex-situ*

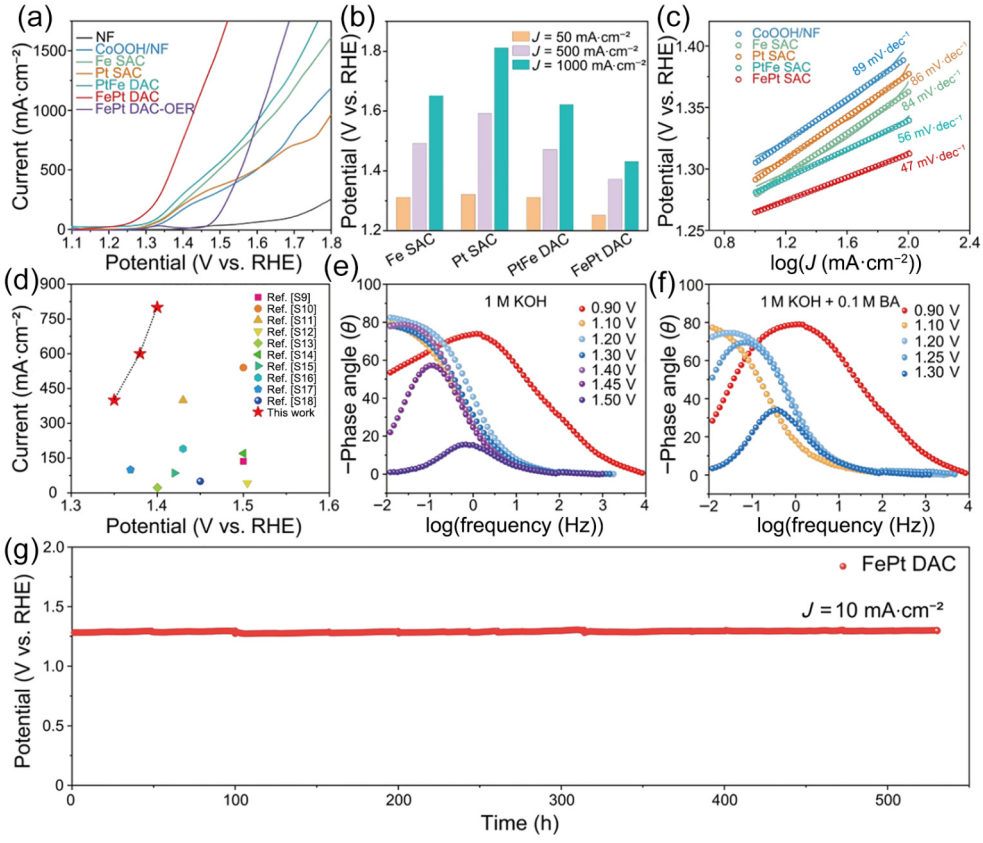

Figure 3 Electrochemical performance of FePt DAC in the 1 M KOH with 0.1 M benzyl alcohol. (a) LSV curves of FePt DAC and other related samples. (b) The corresponding potential at the current density of 50, 500, and 1000 mA·cm^{-2}. (c) Tafel plots derived from BAOR polarization cures in (a). (d) BAOR performance of FePt DAC in comparison with other reported electrocatalysts in references. ((e) and (f)) EIS spectra of FePt DAC in (e) 1 M KOH and (f) 1 M KOH with 0.1 M benzyl alcohol. (g) CP measurement of FePt DAC for 530 h at the current density of 10 mA·cm^{-2}.

Raman spectroscopy revealed that the signal peaks at 480 and 590 cm^{-1} were mainly derived from the oxygen vibrations involving Co–O stretching (A_{1g}) and O–Co–O bending (E_g) vibrations (Fig. S20(a) in the ESM) [52]. These signal peaks were also well-maintained during the entire BAOR process. The peak observed at 1003 cm^{-1} corresponded to the typical signal of benzyl alcohol [53], demonstrating the adsorption of reactant molecules on the surface of FePt DAC, which was crucial for the subsequent activation and reaction of the benzyl alcohol. Besides, the Raman spectra at around 1050 cm^{-1} (Fig. S20(b) in the ESM) assigned to the stretching vibration of O–O$^-$ specie [54, 55] was observed at 1.4 V vs. RHE for FePt DAC when benzyl alcohol was not added into the 1 M KOH solution, suggesting the occurrence of the OER. To probe the evolution of the bonding structure for the key reaction intermediates during BAOR, *in-situ* attenuated total reflection FT infrared spectroscopy (ATR-FTIR) spectra were also performed (Fig. 4(a)). The infrared signals were collected within the wavenumber range from 1000 to 2000 cm^{-1} under electrochemical conditions (potential range from open circuit potential (OCP) to 1.5 V vs. RHE). It should be noted that the obvious infrared band located at around 1695 cm^{-1} was attributed to the M–O* (M = Fe) [56–58] specie, and its vibration intensity increased along with applied potentials from 1.1 to 1.5 V in FePt DAC, which, in contrast to the no M–O* signal detected in the Pt SAC. Besides, Fe SAC catalyst also detected M–O* stretching, which led us to speculate whether water was involved in the BAOR since water oxidation was inevitable in alkaline aqueous solutions. Then, we performed DFT calculations to get insights into the origin of M–O* species. We first selected six model catalysts and calculated the adsorption energies of hydroxide ions on corresponding active sites. As displayed in Fig. S21 in the ESM, for sample co-doped with Fe and Pt (FePt DAC), the adsorption energy of hydroxide ions on the Pt site was the lowest, while the energy required for Co site was the highest. Compared with Pt and Co sites, the adsorption of hydroxide ions on the Fe site possessed the moderate energy. Following, we calculated the OER process occurring on the FePt DAC. As depicted in Fig. 4(b), a large energy barrier of 1.65 eV was required from *OH to *O on the Pt site, while the same process needed 1.32 eV on the Co site. Surprisingly, the energy barrier was only 0.24 eV when *OH was transformed to *O on the Fe site. This significantly reduced energy barrier made it easier for oxygen radicals generated during water oxidation to form on Fe site. Besides, the process from *O to *OOH was greatly suppressed due to the large energy barrier (0.97 eV) on the Fe site. This was consistent with the M–O* bond observed in *in-situ* infrared spectroscopy for Fe–contained samples, which suggested that atomically dispersed Fe atoms may be active site for catalyzing water oxidation in BAOR. In the absence of Fe (Pt SAC), the process of OH* → O* at the Co site still required large energy barrier (1.02 eV), which in contrast to the 0.24 eV on the Fe site in the FePt DAC. This strongly proved the decisive role of Fe site in the BAOR process (Fig. S22 in the ESM). In addition, the adsorption of the reactant benzyl alcohol on the catalyst surface was also crucial. We then compared the distance between α-carbon

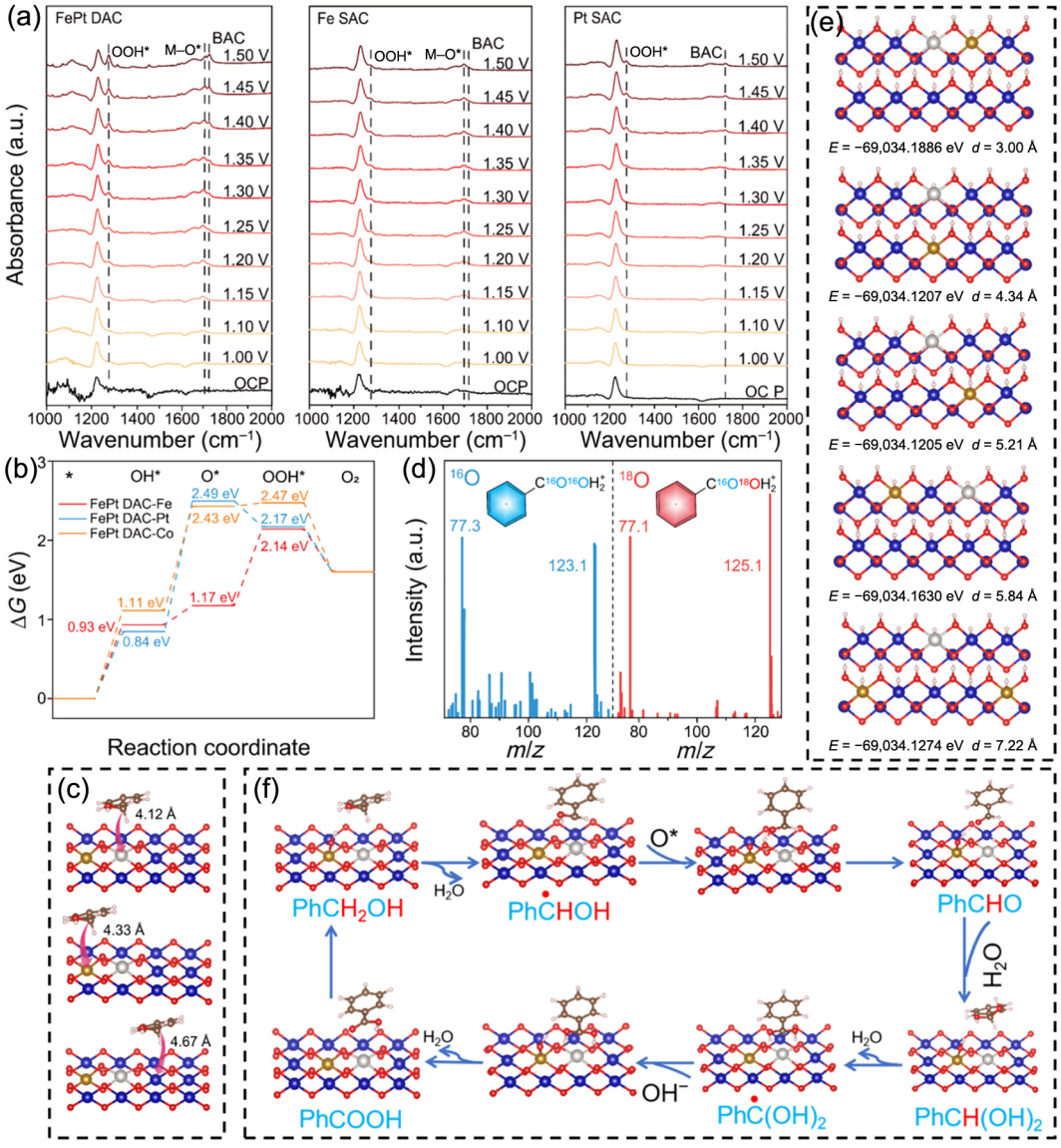

Figure 4 *In-situ* isotope characterization of FePt DAC and theoretical insights into the tandem mechanisms. (a) *In-situ* FTIR spectra of FePt DAC, Fe SAC, and Pt SAC in 1 M KOH with 0.1 M benzyl alcohol. (b) The Gibbs free energy diagram of the OER process on Fe, Pt, and Co sites in FePt DAC. (c) Distance to α-carbon atoms on the benzene ring for adsorption of benzyl alcohol at different sites. (d) Mass spectra (MS) of benzyl alcohol products obtained from the electrocatalytic reaction with ^{16}O and ^{18}O labeled water as oxygen sources, respectively. (e) Five constructed computational models for the FePt DAC with various distance between Fe and Pt atom. The total energies as well as the Fe–Pt distances (d) were listed. (f) Detailed schematic diagram of the tandem reaction occurring on the FePt DAC catalyst. The yellow ball represents the Fe atom, gray ball for Pt atom, indigo ball for Co atom, red ball for O atom, and white ball for H atom.

atoms on the benzene ring in benzyl alcohol and different adsorption site on the FePt DAC catalyst to figure out the adsorption sites of reactant benzyl alcohol (Fig. 4(c) and Figs. S23 and S24 and Table S4 in the ESM). The outcome indicated that benzyl alcohol was prone to be adsorbed on Pt site as compared to Fe and Co sites. Noticeably, the intermediate product benzaldehyde in the reaction was also easily adsorbed on Pt sites, which was conducive to the high selectivity for benzoic acid in BAOR. Besides, the typical OOH* stretching was also detected in FePt DAC when applied voltage was high enough. Based on Fig. 4(b), we inferred that the OOH* may originate from the O* generated on the Fe site being further oxidized [59–61] since the energy barrier demanded for O* to OOH* was only 0.04 eV on the substrate Co site. Meanwhile, the peak at around 1230 cm^{-1} was presented in all three samples, which can be assigned to the stretching mode of benzoic acid product [62, 63]. Notably, the characteristic peak of benzoic acid in FePt DAC appeared earlier (1.2 V) than Fe SAC (1.35 V) and Pt SAC (1.35 V), which was in good accordance with the electrochemical test results.

Then, we applied isotopic experiment in which ^{18}O-labeled water ($H_2{}^{18}O$) was used to identify the oxygen source in the ultimate product benzoic acid. As displayed in Fig. 4(d), for the products obtained in $H_2{}^{16}O$/KOH, the peak with a mass-to-charge ratio (*m*/*z*) of 123.1 was attributed to the molecular ion of protonated benzoic acid (C_6H_5-$C^{16}O^{16}OH^{2+}$). The peak located at 77.1 was the signal of C_6H_5-ion fragments, corresponding to the benzene molecule with a substituent lost [64]. When heavy oxygen water $H_2{}^{18}O$ was added to the system, the characteristic product peak shifted to a higher *m*/*z* of 125.1 due to the introduction of the ^{18}O atom. As a result, water molecules participate in the oxidation of benzyl alcohol. The above

data inspired us to think that atomically dispersed Fe and Pt seemingly combined to play a synergistic role in the BAOR and were closely related to the efficient benzoic acid generation. Subsequently, we constructed five computational models for the FePt DAC with various atomic distances between Fe and Pt atoms to further explore the stable structure of atomically dispersed Fe and Pt in catalysts (Fig. 4(e)). The calculation results indicated that Fe and Pt atoms were thermodynamically stable when they were in adjacent positions with a spacing of 3.0 Å. On this basis, we hypothesized that the successful fabrication of Fe–Pt dual atomic sites on the CoOOH substrate may be attributed to the superior water coupled BAOR performance, in which the coupling of O* and adsorbed benzyl alcohol played a key role in the efficient generation of benzoic acid. Specifically, the Fe sites in Fe–Pt dual atomic sites promoted water oxidation with oxidative free radicals, which further oxidized benzyl alcohol that adsorbed on the surface of the catalyst, thereby synergistically catalyzing the production of benzoic acid. Based on the above theoretical calculations and analysis, we speculated that the reaction pathways during BAOR were probed in detail as following five steps (Fig. 4(f)): (1) Firstly, the adsorption of the OH^- in the alkaline aqueous solution onto the Fe site in FePt DAC caused the dehydrogenation of benzyl alcohol that adsorbed on the adjacent Pt site, resulting PhĊHOH and H_2O. (2) Then the O* generated on the Fe site through water oxidation further oxidized the PhĊHOH that still adsorbed on the Pt site to PhCHO, with O* being *in-situ* reduced to OH* on the Fe site. (3) The intermediate product PhCHO immediately underwent hydration in solution to form $PhĊH(OH)_2$. (4) The hydrated $PhĊH(OH)_2$ reacted with OH* forming $PhĊ(OH)_2$. (5) Finally, the OH^- in the solution participated in the subsequent hydroxyl dehydrogenation of the $PhĊ(OH)_2$ intermediate to form ultimate product benzoic acid. The elementary electrochemical steps considered for the tandem process are shown as following

$$\text{Step1: } PhCH_2OH + OH^- \rightarrow PhĊHOH + H_2O + e^-$$

$$\text{Step2: } PhĊHOH + O^* \rightarrow PhCHO + OH^*$$

$$\text{Step3: } PhCHO + H_2O \rightarrow PhCH(OH)_2$$

$$\text{Step4: } PhĊH(OH)_2 + OH^* \rightarrow PhĊ(OH)_2 + H_2O$$

$$\text{Step5: } PhĊ(OH)_2 + OH^- \rightarrow PhCOOH + H_2O + e^-$$

According to the proposed tandem reaction mechanism (Step 2: PhĊHOH + O* → PhCHO + OH*), the reaction between deprotonated benzyl alcohol on Pt sites and reactive oxygen species on Fe sites, was achieved through hydrogen bonding, as shown in Fig. S25 in the ESM. That is to say, hydrogen bonding occurred when Fe and Pt atoms were separated by a distance of 3.0 Å. It would not be hydrogen bonds when atomic distance longer than 3.0 Å. This conclusion also supported the speculation and demonstration of atomic spacing in FePt DAC catalysts.

2.5 Flow cell measurements and schematic illustration of the BAOR and product separation

To evaluate the catalyst in a more practical application situations, we carried out two-electrode tests in a flow electrolyte using FePt DAC catalyst as anode and Ni foam as cathode with working area of 4 cm^2 (Fig. 5(a)). The 2 M KOH that contained 0.3 M benzyl

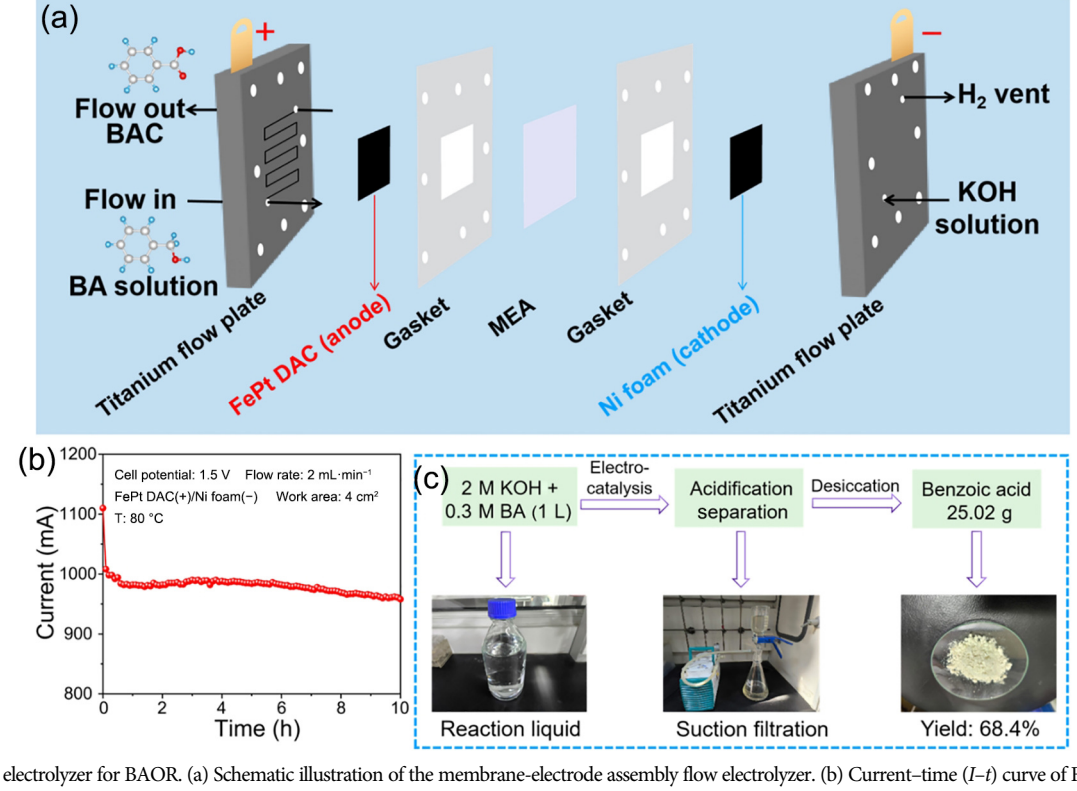

Figure 5 Flow electrolyzer for BAOR. (a) Schematic illustration of the membrane-electrode assembly flow electrolyzer. (b) Current–time (*I*–*t*) curve of FePt DAC (+)||Ni foam (−) at 1.5 V in a 2 M KOH with 0.3 M benzyl alcohol in the membrane-electrode assembly flow electrolyzer. (c) Schematic illustration of the BAOR process and product separation.

alcohol and 2 M KOH solutions were injected into the anode and cathode of the flow electrolyzer at the flow rate of 2 mL·min^{-1}, respectively (Fig. S26 in the ESM). The system achieved excellent BAOR activity with about 1000 mA at 1.5 V cell potential (Fig. 5(b)). Subsequently, the reaction solution was then acidified, filtered, and dried to obtain high-purity benzoic acid production. Finally, the yield of benzoic acid was calculated to be 68.4% (Fig. 5(c)).

3 Conclusions

In summary, we have constructed a dual atomic site catalyst with adjacent Fe–Pt dual atomic sites homogeneously dispersed on CoOOH nanosheet arrays via electrodeposition (FePt DAC). The FePt DAC catalyst manifests outstanding activity and durability for BAOR. Experimental analysis and DFT calculations reveal the cooperation between adjacent Fe and Pt atoms, in which the oxygen radicals generated on the Fe site through OER directly react with the absorbed benzyl alcohol on the neighboring Pt atom. This work provides valuable insights into the pivotal role of active oxygen species derived from water electrolysis in electrooxidation of organic compounds into high value-added chemicals.

Electronic Supplementary Material: Supplementary material (electrochemical test methods, *in-situ* ATR surface enhanced infrared absorption spectroscopy (ATR-SEIRAS), *in-situ* Raman spectroscopy measurement, and calculation details) is available in the online version of this article at https://doi.org/10.26599/NR.2025.94907362.

Data availability

All data needed to support the conclusions in the paper are presented in the manuscript and the Electronic Supplementary Material. Additional data related to this paper may be requested from the corresponding author upon request.

Acknowledgements

This work was financially supported by the National Natural Science Foundation of China (Nos. 22375131, 52172096, and 22405180). The authors also thank the BL11B station in the Shanghai Synchrotron Radiation Facility (SSRF) and the 1W1B station in the Beijing Synchrotron Radiation Facility (BSRF) for help with XAS spectra.

Declaration of competing interest

All the contributing authors report no conflict of interests in this work.

Author contribution statement

G. H. S.: Designed research, performed research, analyzed data, wrote the paper. W. M. S.: Analyzed data. X. L. W.: Analyzed data, wrote the paper. S. Y. G.: Analyzed data. Y. T.: Designed research, wrote the paper. All the authors have approved the final manuscript.

Use of AI statement

None.

References

[1] Shih, A. J.; Monteiro, M. C. O.; Dattila, F.; Pavesi, D.; Philips, M.; da Silva, A. H. M.; Vos, R. E.; Ojha, K.; Park, S.; van der Heijden, O. et al. Water electrolysis. *Nat. Rev. Methods Primers* **2022**, *2*, 84.

[2] Zhang, H. H.; Fu, Y.; Nguyen, H. T.; Fox, B.; Lee, J. H.; Lau, A. K. T.; Zheng, H.; Lin, H.; Ma, T. Y.; Jia, B. H. Material challenges in green hydrogen ecosystem. *Coord. Chem. Rev.* **2023**, *494*, 215272.

[3] Seh, Z. W.; Kibsgaard, J.; Dickens, C. F.; Chorkendorff, I.; Nørskov, J. K.; Jaramillo, T. F. Combining theory and experiment in electrocatalysis: Insights into materials design. *Science* **2017**, *355*, eaad4998.

[4] Wang, X. L.; Xiao, H.; Li, A.; Li, Z.; Liu, S. J.; Zhang, Q. H.; Gong, Y.; Zheng, L. R.; Zhu, Y. Q.; Chen, C. et al. Constructing NiCo/Fe_3O_4 heteroparticles within MOF-74 for efficient oxygen evolution reactions. *J. Am. Chem. Soc.* **2018**, *140*, 15336–15341.

[5] Mu, X. Q.; Yuan, Y. T.; Yu, M.; Hu, Y. J.; Zeng, W. H.; Peng, W.; Zhang, Y. F.; Liu, X. Y.; Liu, S. L.; Mu, S. C. Robust water/seawater-electrolysis hydrogen production at industrial-scale current densities by modulating built-in-outer electric field of catalytic substance. *Nano Energy* **2024**, *131*, 110216.

[6] Zhang, H. C.; Li, C. S.; Lu, Q.; Cheng, M. J.; Goddard III, W. A. Selective activation of propane using intermediates generated during water oxidation. *J. Am. Chem. Soc.* **2021**, *143*, 3967–3974.

[7] Tang, H. T.; Zhou, H. Y.; Pan, Y. M.; Zhang, J. L.; Cui, F. H.; Li, W. H.; Wang, D. S. Single-atom manganese-catalyzed oxygen evolution drives the electrochemical oxidation of silane to silanol. *Angew. Chem., Int. Ed.* **2024**, *63*, e202315032.

[8] Liu, F. L.; Gao, X. T.; Shi, R.; Guo, Z. X.; Tse, E. C. M.; Chen, Y. Concerted and selective electrooxidation of polyethylene-terephthalate-derived alcohol to glycolic acid at an industry-level current density over a Pd–Ni$(OH)_2$ catalyst. *Angew. Chem., Int. Ed.* **2023**, *62*, e202300094.

[9] Zhang, Y.; Mu, X. Q.; Liu, Z. Y.; Zhao, H. Y.; Zhuang, Z. C.; Zhang, Y. F.; Mu, S. C.; Liu, S. L.; Wang, D. S.; Dai, Z. H. Twin-distortion modulated ultra-low coordination PtRuNi–O_x catalyst for enhanced hydrogen production from chemical wastewater. *Nat. Commun.* **2024**, *15*, 10149.

[10] Mu, X. Q.; Zhang, X. Y.; Chen, Z. Y.; Gao, Y.; Yu, M.; Chen, D.; Pan, H. Z.; Liu, S. L.; Wang, D. S.; Mu, S. C. Constructing symmetry-mismatched $Ru_xFe_{3-x}O_4$ heterointerface-supported Ru clusters for efficient hydrogen evolution and oxidation reactions. *Nano Lett.* **2024**, *24*, 1015–1023.

[11] Zhou, H.; Li, Z. H.; Xu, S. M.; Lu, L. L.; Xu, M.; Ji, K. Y.; Ge, R. X.; Yan, Y. F.; Ma, L. N.; Kong, X. G. et al. Selectively upgrading lignin derivatives to carboxylates through electrochemical oxidative C(OH)–C bond cleavage by a Mn-doped cobalt oxyhydroxide catalyst. *Angew. Chem., Int. Ed.* **2021**, *60*, 8976–8982.

[12] Chen, Y. X.; Lavacchi, A.; Miller, H. A.; Bevilacqua, M.; Filippi, J.; Innocenti, M.; Marchionni, A.; Oberhauser, W.; Wang, L.; Vizza, F. Nanotechnology makes biomass electrolysis more energy efficient than water electrolysis. *Nat. Commun.* **2014**, *5*, 4036.

[13] Zhao, Y. K.; Deng, C. Y.; Tang, D. J.; Ding, L. Y.; Zhang, Y. C.; Sheng, H.; Ji, H. W.; Song, W. J.; Ma, W. H.; Chen, C. C. et al. α-Fe_2O_3 as a versatile and efficient oxygen atom transfer catalyst in combination with H_2O as the oxygen source. *Nat. Catal.* **2021**, *4*, 684–691.

[14] Lu, Y. X.; Chen, M. Y.; Wang, Y. Q.; Yang, C. M.; Zou, Y. Q.; Wang, S. Y. Aqueous electrocatalytic small-molecule valorization trilogy. *Chem* **2024**, *10*, 1371–1390.

[15] Liu, C. B.; Chen, F. P.; Zhao, B. H.; Wu, Y. M.; Zhang, B. Electrochemical hydrogenation and oxidation of organic species involving water. *Nat. Rev. Chem.* **2024**, *8*, 277–293.

[16] Huang, H. L.; Yu, C.; Han, X. T.; Huang, H. W.; Wei, Q. B.; Guo, W.; Wang, Z.; Qiu, J. S. Ni, Co hydroxide triggers electrocatalytic

production of high-purity benzoic acid over 400 mA·cm^{-2}. *Energy Environ. Sci.* **2020**, *13*, 4990–4999.
[17] Qin, Y. L.; Yu, K. D.; Wang, G.; Zhuang, Z. C.; Dou, Y. H.; Wang, D. S.; Chen, Z. B. Adjacent-ligand tuning of atomically precise Cu–Pd sites enables efficient methanol electrooxidation with a CO-free pathway. *Angew. Chem., Int. Ed.* **2025**, *64*, e202420817.
[18] Li, Z. H.; Yan, Y. F.; Xu, S. M.; Zhou, H.; Xu, M.; Ma, L. N.; Shao, M. F.; Kong, X. G.; Wang, B.; Zheng, L. R. et al. Alcohols electrooxidation coupled with H_2 production at high current densities promoted by a cooperative catalyst. *Nat. Commun.* **2022**, *13*, 147.
[19] Yin, Z.; Zheng, Y. M.; Wang, H.; Li, J. X.; Zhu, Q. J.; Wang, Y.; Ma, N.; Hu, G.; He, B. Q.; Knop-Gericke, A. et al. Engineering interface with one-dimensional Co_3O_4 nanostructure in catalytic membrane electrode: Toward an advanced electrocatalyst for alcohol oxidation. *ACS Nano* **2017**, *11*, 12365–12377.
[20] Chen, W.; Xie, C.; Wang, Y. Y.; Zou, Y. Q.; Dong, C. L.; Huang, Y. C.; Xiao, Z. H.; Wei, Z. X.; Du, S. Q.; Chen, C. et al. Activity origins and design principles of nickel-based catalysts for nucleophile electrooxidation. *Chem* **2020**, *6*, 2974–2993.
[21] Bender, M. T.; Lam, Y. C.; Hammes-Schiffer, S.; Choi, K. S. Unraveling two pathways for electrochemical alcohol and aldehyde oxidation on NiOOH. *J. Am. Chem. Soc.* **2020**, *142*, 21538–21547.
[22] Li, Y. P.; Niu, S. W.; Liu, P. G.; Pan, R. R.; Zhang, H. K.; Ahmad, N.; Shi, Y.; Liang, X.; Cheng, M. Y.; Chen, S. H. et al. Ruthenium nanoclusters and single atoms on α-MoC/N-doped carbon achieves low-input/input-free hydrogen evolution via decoupled/coupled hydrazine oxidation. *Angew. Chem., Int. Ed.* **2024**, *63*, e202316755.
[23] Qiao, B. T.; Wang, A. Q.; Yang, X. F.; Allard, L. F.; Jiang, Z.; Cui, Y. T.; Liu, J. Y.; Li, J.; Zhang, T. Single-atom catalysis of CO oxidation using Pt_1/FeO_x. *Nat. Chem.* **2011**, *3*, 634–641.
[24] Liu, L. C.; Corma, A. Metal catalysts for heterogeneous catalysis: From single atoms to nanoclusters and nanoparticles. *Chem. Rev.* **2018**, *118*, 4981–5079.
[25] Chen, Y. J.; Ji, S. F.; Chen, C.; Peng, Q.; Wang, D. S.; Li, Y. D. Single-atom catalysts: Synthetic strategies and electrochemical applications. *Joule* **2018**, *2*, 1242–1264.
[26] Wang, L. G.; Wu, J. B.; Wang, S. W.; Liu, H.; Wang, Y.; Wang, D. S. The reformation of catalyst: From a trial-and-error synthesis to rational design. *Nano Res.* **2024**, *17*, 3261–3301.
[27] Zhuang, J. H.; Wang, D. S. Recent advances of single-atom alloy catalyst: Properties, synthetic methods and electrocatalytic applications. *Mater. Today Catal.* **2023**, *2*, 100009.
[28] Ying, Y. R.; Luo, X.; Qiao, J. L.; Huang, H. T. "More is different:" Synergistic effect and structural engineering in double-atom catalysts. *Adv. Funct. Mater.* **2021**, *31*, 2007423.
[29] Wang, X. L.; Fu, N. H.; Liu, J. C.; Yu, K.; Li, Z.; Xu, Z. F.; Liang, X.; Zhu, P.; Ye, C. L.; Zhou, A. et al. Atomic replacement of PtNi nanoalloys within Zn-ZIF-8 for the fabrication of a multisite CO_2 reduction electrocatalyst. *J. Am. Chem. Soc.* **2022**, *144*, 23223–23229.
[30] Gan, T.; Wang, D. S. Atomically dispersed materials: Ideal catalysts in atomic era. *Nano Res.* **2024**, *17*, 18–38.
[31] Wang, Y.; Ma, F. Y.; Zhang, G. Q.; Zhang, J. W.; Zhao, H.; Dong, Y. M.; Wang, D. S. Precise synthesis of dual atom sites for electrocatalysis. *Nano Res.* **2024**, *17*, 9397–9427.
[32] Wang, L. G.; Su, H.; Tan, G. Y.; Xin, J. J.; Wang, X. G.; Zhang, Z.; Li, Y. P.; Qiu, Y.; Li, X. H.; Li, H. S. et al. Boosting efficient and sustainable alkaline water oxidation on a W-CoOOH-TT pair-sites catalyst synthesized via topochemical transformation. *Adv. Mater.* **2024**, *36*, 2302642.
[33] Gao, Y.; Yang, C. D.; Sun, F. L.; He, D. P.; Wang, X. Q.; Chen, J.; Zheng, X. B.; Liu, R. C.; Pan, H. G.; Wang, D. S. Ligand-tuning metallic sites in molecular complexes for efficient water oxidation. *Angew. Chem., Int. Ed.* **2025**, *64*, e202415755.
[34] Mu, X. Q.; Liu, S. L.; Zhang, M. Y.; Zhuang, Z. C.; Chen, D.; Liao, Y. R.; Zhao, H. Y.; Mu, S. C.; Wang, D. S.; Dai, Z. H. Symmetry-broken Ru nanoparticles with parasitic Ru–Co dual-single atoms overcome the volmer step of alkaline hydrogen oxidation. *Angew. Chem., Int. Ed.* **2024**, *63*, e202319618.
[35] Guo, Y. J.; Liu, Z. Y.; Zhou, D. Y.; Zhang, M. Y.; Zhang, Y.; Li, R. Z.; Liu, S. L.; Wang, D. S.; Dai, Z. H. Competition and synergistic effects of Ru-based single-atom and cluster catalysts in electrocatalytic reactions. *Sci. China Mater.* **2024**, *67*, 1706–1720.
[36] Zhang, Z. D.; Zhu, J. X.; Chen, S. H.; Sun, W. M.; Wang, D. S. Liquid fluxional Ga single atom catalysts for efficient electrochemical CO_2 reduction. *Angew. Chem., Int. Ed.* **2023**, *62*, e202215136.
[37] Zhang, W. Y.; Chao, Y. G.; Zhang, W. S.; Zhou, J. H.; Lv, F.; Wang, K.; Lin, F. X.; Luo, H.; Li, J.; Tong, M. P. et al. Emerging dual-atomic-site catalysts for efficient energy catalysis. *Adv. Mater.* **2021**, *33*, 2102576.
[38] Sun, M. Z.; Wong, H. H.; Wu, T.; Dougherty, A. W.; Huang, B. L. Stepping out of transition metals: Activating the dual atomic catalyst through main group elements. *Adv. Energy Mater.* **2021**, *11*, 2101404.
[39] Zhu, P.; Xiong, X.; Wang, D. S.; Li, Y. D. Advances and regulation strategies of the active moiety in dual-atom site catalysts for efficient electrocatalysis. *Adv. Energy Mater.* **2023**, *13*, 2300884.
[40] Wang, L. G.; Su, H.; Zhang, Z.; Xin, J. J.; Liu, H.; Wang, X. G.; Yang, C. Y.; Liang, X.; Wang, S. W.; Liu, H. et al. Co–Co dinuclear active sites dispersed on zirconium-doped heterostructured Co_9S_8/Co_3O_4 for high-current-density and durable acidic oxygen evolution. *Angew. Chem., Int. Ed.* **2023**, *62*, e202314185.
[41] Wang, J.; Liu, W.; Luo, G.; Li, Z. J.; Zhao, C.; Zhang, H. R.; Zhu, M. Z.; Xu, Q.; Wang, X. Q.; Zhao, C. M. et al. Synergistic effect of well-defined dual sites boosting the oxygen reduction reaction. *Energy Environ. Sci.* **2018**, *11*, 3375–3379.
[42] Kim, U. B.; Jung, D. J.; Jeon, H. J.; Rathwell, K.; Lee, S. G. Synergistic dual transition metal catalysis. *Chem. Rev.* **2020**, *120*, 13382–13433.
[43] Hu, Y. F.; Li, Z. S.; Li, B. L.; Yu, C. L. Recent progress of diatomic catalysts: General design fundamentals and diversified catalytic applications. *Small* **2022**, *18*, 2203589.
[44] Li, Y. Z.; Wei, B.; Zhu, M. H.; Chen, J. C.; Jiang, Q. K.; Yang, B.; Hou, Y.; Lei, L. C.; Li, Z. J.; Zhang, R. F. et al. Synergistic effect of atomically dispersed Ni–Zn pair sites for enhanced CO_2 electroreduction. *Adv. Mater.* **2021**, *33*, 2102212.
[45] Sun, Y. F.; Sun, Z. H.; Gao, S.; Cheng, H.; Liu, Q. H.; Piao, J. Y.; Yao, T.; Wu, C. Z.; Hu, S. L.; Wei, S. Q. et al. Fabrication of flexible and freestanding zinc chalcogenide single layers. *Nat. Commun.* **2012**, *3*, 1057.
[46] Feng, C.; Zhang, Z. R.; Wang, D. D.; Kong, Y.; Wei, J.; Wang, R. Y.; Ma, P. Y.; Li, H. L.; Geng, Z. G.; Zuo, M. et al. Tuning the electronic and steric interaction at the atomic interface for enhanced oxygen evolution. *J. Am. Chem. Soc.* **2022**, *144*, 9271–9279.
[47] Moysiadou, A.; Lee, S.; Hsu, C. S.; Chen, H. M.; Hu, X. L. Mechanism of oxygen evolution catalyzed by cobalt oxyhydroxide: Cobalt superoxide species as a key intermediate and dioxygen release as a rate-determining step. *J. Am. Chem. Soc.* **2020**, *142*, 11901–11914.
[48] Zhang, T. Y.; Jiang, J. J.; Sun, W. M.; Gong, S. Y.; Liu, X. W.; Tian, Y.; Wang, D. S. Spatial configuration of Fe–Co dual-sites boosting catalytic intermediates coupling toward oxygen evolution reaction. *Proc. Natl. Acad. Sci. USA* **2024**, *121*, e2317247121.
[49] Chen, W.; Wang, Y. Y.; Wu, B. B.; Shi, J. Q.; Li, Y. Y.; Xu, L. T.; Xie, C.; Zhou, W.; Huang, Y. C.; Wang, T. H. et al. Activated Ni–OH bonds in a catalyst facilitates the nucleophile oxidation reaction. *Adv. Mater.* **2022**, *34*, 2105320.
[50] Qi, Y. B.; Zhang, Y.; Yang, L.; Zhao, Y. H.; Zhu, Y. H.; Jiang, H. L.; Li, C. Z. Insights into the activity of nickel boride/nickel heterostructures for efficient methanol electrooxidation. *Nat. Commun.* **2022**, *13*, 4602.
[51] Wang, H. Y.; Hung, S. F.; Chen, H. Y.; Chan, T. S.; Chen, H. M.; Liu, B. In *operando* identification of geometrical-site-dependent water oxidation activity of spinel Co_3O_4. *J. Am. Chem. Soc.* **2016**, *138*, 36–39.

[52] Zheng, X. B.; Chen, Y. P.; Zheng, X. S.; Zhao, G. Q.; Rui, K.; Li, P.; Xu, X.; Cheng, Z. X.; Dou, S. X.; Sun, W. P. Electronic structure engineering of $LiCoO_2$ toward enhanced oxygen electrocatalysis. *Adv. Energy Mater.* **2019**, *9*, 1803482.
[53] Li, R. C.; Kuang, P. Y.; Wageh, S.; Al-Ghamdi, A. A.; Tang, H. L.; Yu, J. G. Potential-dependent reconstruction of Ni-based cuboid arrays for highly efficient hydrogen evolution coupled with electro-oxidation of organic compound. *Chem. Eng. J.* **2023**, *453*, 139797.
[54] Huang, Y.; Wang, Z. Y.; Xiao, H.; Liu, Q. D.; Wang, X. Activating and stabilizing lattice oxygen via self-adaptive Zn–NiOOH sub-nanowires for oxygen evolution reaction. *J. Am. Chem. Soc.* **2024**, *146*, 29006–29016.
[55] Zhu, K. Y.; Zhu, X. F.; Yang, W. S. Application of *in-situ* techniques for the characterization of NiFe-based oxygen evolution reaction (OER) electrocatalysts. *Angew. Chem., Int. Ed.* **2019**, *58*, 1252–1265.
[56] Hu, Y.; Zheng, Y.; Jin, J.; Wang, Y. T.; Peng, Y.; Yin, J.; Shen, W.; Hou, Y. C.; Zhu, L.; An, L. et al. Understanding the sulphur–oxygen exchange process of metal sulphides prior to oxygen evolution reaction. *Nat. Commun.* **2023**, *14*, 1949.
[57] Sun, X.; Zhang, X. X.; Li, Y. L.; Xu, Y. Z.; Su, H.; Che, W.; He, J. F.; Zhang, H.; Liu, M. H.; Zhou, W. L. et al. *In-situ* construction of flexible V–Ni redox centers over Ni-based MOF nanosheet arrays for electrochemical water oxidation. *Small Methods* **2021**, *5*, 2100573.
[58] Li, Y. L.; Cheng, W. R.; Su, H.; Zhao, X.; He, J. F.; Liu, Q. H. *Operando* infrared spectroscopic insights into the dynamic evolution of liquid–solid (photo)electrochemical interfaces. *Nano Energy* **2020**, *77*, 105121.
[59] Liao, P. L.; Keith, J. A.; Carter, E. A. Water oxidation on pure and doped hematite (0001) surfaces: Prediction of Co and Ni as effective dopants for electrocatalysis. *J. Am. Chem. Soc.* **2012**, *134*, 13296–13309.
[60] Viswanathan, V.; Hansen, H. A.; Nørskov, J. K. Selective electrochemical generation of hydrogen peroxide from water oxidation. *J. Phys. Chem. Lett.* **2015**, *6*, 4224–4228.
[61] Xia, C.; Back, S.; Ringe, S.; Jiang, K.; Chen, F. H.; Sun, X. M.; Siahrostami, S.; Chan, K. R.; Wang, H. T. Confined local oxygen gas promotes electrochemical water oxidation to hydrogen peroxide. *Nat. Catal.* **2020**, *3*, 125–134.
[62] Wang, K. P.; Huang, J. S.; Hu, J. G.; Wu, M.; Liao, Y. H.; Yang, S.; Li, H. Visible light-switchable lattice oxygen sites for selective C–H and C(O)–C bond electrooxidation. *Angew. Chem., Int. Ed.* **2024**, *63*, e202410555.
[63] Luo, D. C.; Tang, Z. Y.; Yu, X. Y.; Zhang, T.; Chang, C. R.; Hu, Z. Revealing the ZrO_2 crystal effect of Pd/ZrO_2 catalyst for toluene combustion: A combined DRIFTS and DFT study. *Appl. Catal. B Environ.* **2023**, *339*, 123117.
[64] Dang, K.; Dong, H. L.; Wang, L. G.; Jiang, M.; Jiang, S.; Sun, W. M.; Wang, D. S.; Tian, Y. Boosting electrochemical styrene transformation via tandem water oxidation over a single-atom $Cr_1/CoSe_2$ catalyst. *Adv. Mater.* **2022**, *34*, 2200302.